The Thermocapillary Effect on Gas Bubbles Growing on Electrodes of Different Sizes

Hossain, S. S.; Mutschke, G.; Bashkatov, A.; Eckert, K.;

Originally published:

June 2020

Electrochimica Acta 353(2020), 136461

DOI: https://doi.org/10.1016/j.electacta.2020.136461

Perma-Link to Publication Repository of HZDR:

https://www.hzdr.de/publications/Publ-30979

The thermocapillary effect on gas bubbles growing on electrodes of different sizes

Syed Sahil Hossain[a], Gerd Mutschke[a,*], Aleksandr Bashkatov[a], Kerstin Eckert[a,b]

[a] *Institute of Fluid Dynamics, Helmholtz-Zentrum Dresden-Rossendorf, Bautzner Landstrasse 400, Dresden, 01328 Germany*
[b] *Institute of Process Engineering and Environmental Technology, Technische Universität Dresden, Dresden, 01062 Germany*

Abstract

Recently, the strongly inhomogeneous current density occuring near a microelectrode was identified as driving a thermocapillary electrolyte flow near gas bubbles growing during electrolysis [1]. The present paper is investigating this effect in more detail under various operating conditions. Furthermore, by simplified modeling, the question is answered of whether this effect is also of importance at large planar electrodes. The direction of the thermocapillary force on the bubble is found to change from retarding to advancing the bubble release when the size of the electrode is increased. Conclusions are drawn on how the thermocapillary effect at planar electrodes depends on the electrode coverage and the bubble departure size, also considering industrially relevant values of the current density.

Keywords: hydrogen evolution, electrolysis, thermocapillarity, Marangoni force, microelectrode, macroelectrode

1. Introduction

Interfaces between media of different phases are ubiquitous in nature and play an important role in many physico-chemical systems. If liquids are involved, capillary effects often influence the system behavior [2]. The surface tension for a given liquid-gas pair is known to depend on physical properties of the interface, namely the temperature, chemical composition and electric potential in the presence of interfacial charge [3]. Thus, interfacial gradients of these physical properties cause the surface tension to vary along the interface. As a result, due to unbalanced forces at the interface, fluid elements there experience a net shear stress and move towards interface regions of higher interfacial tension. The resulting capillary flow is commonly called Marangoni flow [4]. This Marangoni effect is known to occur in many systems of scientific and technological importance. For example, thermo-capillarity is the mechanism which drives the well-known Bénard cells ([5–7] and references therein), a phenomenon occurring in many engineering heat transfer applications. In liquid-liquid extraction processes, soluto-capillary flows may significantly change the mass transfer rate

*Corresponding author: g.mutschke@hzdr.de

[8]. Furthermore, Marangoni flow exists at sessile evaporating droplets due to the interfacial temperature gradient caused by a nonuniform rate of evaporation [9]. This influences the well-known coffee-ring-like structures [10], and may thus affect patterned deposition [11] and particle self-assembly [12].

In 1959, Young et al. [13] demonstrated the profound effect which Marangoni flow can have on air bubbles in liquids by applying a positive temperature gradient in the direction of gravity to suspend them against buoyancy. The temperature gradient induced a surface tension gradient along the bubble interface and thus exerted a thermocapillary stress on the interface, which caused the bubble to experience a force against buoyancy. At a sufficiently steep temperature gradient, the thermocapillary force can be as large as buoyancy. Later, with the advent of space research, bubble actuation in micro-gravity by means of thermocapillarity attracted much interest [14, 15]. Experiments conducted in the space shuttle in orbit showed that by applying a temperature gradient of the order of 1 K/mm, a bubble migration speed of $\sim$1mm/s could be achieved for a bubble of millimeter size [16]. McGrew et al. [17] speculated that Marangoni convection might have a significant contribution to heat transfer in nucleate boiling, as the observed flow structure around a pendant air bubble heated from above was found to be similar to that of a vapor bubble during boiling. Later, in nucleate boiling experiments conducted under microgravity conditions, the heat transfer rate obtained by Straub was similar to that obtained under normal gravity conditions [18], which lent further credence to the importance of Marangoni flow around the bubbles. Further experiments and numerical simulations [19–21] established the significant importance of thermocapillarity-driven flow in the subcooled boiling regime and showed that the resulting Marangoni force acting on the bubble slowed down their detachment from the boiling surface [22].

It has long been hypothesised that the Marangoni effect also influences the dynamics of bubbles grown electrochemically on electrodes [23, 24]. Definitive experimental evidence of the Marangoni effect was first provided by Yang et al. [25], who performed a detailed investigation of the interfacial flow around hydrogen bubbles grown on a Platinum microelectrode. Then, by simultaneously measuring the electrolyte velocity and temperature and correlating the results with the numerical solution obtained when considering only thermocapillarity, Massing et al. [1] were able to show that the Marangoni flow observed is primarily attributed to the thermocapillary effect caused by the temperature gradient along the bubble interface. Interestingly, for strong local boiling at microheaters, the thermocapillary flow found near the gas bubble qualitatively matches the flow structure near the electrogenerated gas bubble at a microelectrode [1], though due to strong laser heating the maximum flow velocity is about 10 times higher [26].

As gas bubbles are generated in many electrochemical processes such as plating, refining of metal or the chloralkali process [27–29], a better understanding of the dynamics of electrogenerated bubbles and associated thermo-fluidic phenomena is of great technological and scientific interest. This is particularly relevant for H_2 production through water electrolysis, as the bubble evolution rate directly influences both the system throughput and the process efficiency [30], which may be of increasing importance for next-

generation green energy storage and mobility applications [31–33].

As bubbles attached to the electrode surface disturb a homogeneous surface reaction rate, reduce the active reaction area and increase the electrical resistance of the cell, the speedy removal of generated bubbles from the electrode surface is highly desirable with respect to both deposit quality and electrical efficiency. The instant of bubble departure and the departing diameter is determined by the equilibrium of forces acting on the bubble [34]. However, the often-used Fritz equation [35] does not provide an accurate prediction of the departure diameter [36]. For the special case of oxygen bubbles grown photocatalytically on TiO_2 nanorods where a temperature gradient is caused by light irradiation, Chen et al. have recently shown that the inclusion of both thermocapillary and solutal Marangoni forces in the force balance of the bubble could considerably improve the estimate of the bubble departure [37]. However, beside the aforementioned study by Massing et al. [1], where a retarding influence of the thermocapillary effect on the bubble departure was found, no systematic study has been carried out for electrogenerated bubbles.

For studying bubble evolution during electrolysis, microscale electrodes have been widely used, as the nucleation area is limited, and single bubble growth can be more easily observed compared to the spatially random nucleation occuring at large planar electrodes [38–41]. The recent work which was the first to confirm the existence of thermocapillary flow around electrogenerated bubbles [1] was also carried out at microelectrodes. However, there remains a need for more detailed investigations of this phenomenon. In particular, the question has not yet been addressed of whether this effect is also of importance at the larger electrodes, which are more relevant to industrial applications. Therefore, in this study we perform detailed numerical simulations and analyses of the thermocapillary effect at electrogenerated bubbles on electrodes of varying size. Different operating conditions are investigated, and the important qualitative differences found between microelectrodes and macroelectrodes will be emphasized.

2. Simulation setup

Microelectrode. To study the thermocapillary effect around a hydrogen bubble at a microelectrode of varying size, our simulation setup closely follows the methodology used by Massing et al. [1]. A cylindrical electrochemical cell with a radius $R_c = 5$ mm and a height $R_h = 5$ mm is considered. It is filled with an aqueous solution of 1 M H_2SO_4. The computational domain is sketched in Figure 1a. At the bottom of the cell, a bubble with a radius $R_b = 560$ μm sits on a Pt microelectrode (radius R_e), which works as the cathode. The contact angle between the bubble and electrode is $\theta_c = 4.2°$ [1]. It should be noted here that the bubble radius is much smaller than the size of the cell. The Pt microelectrode is embedded in a glass bottom. The top of the cell is completely covered by a counter-electrode made of platinum. The electrodes and the glass bottom have a height of 5 mm each. The inclusion of the glass bottom and both electrode domains is important for an accurate calculation of the temperature field in the electrolyte due to non-zero

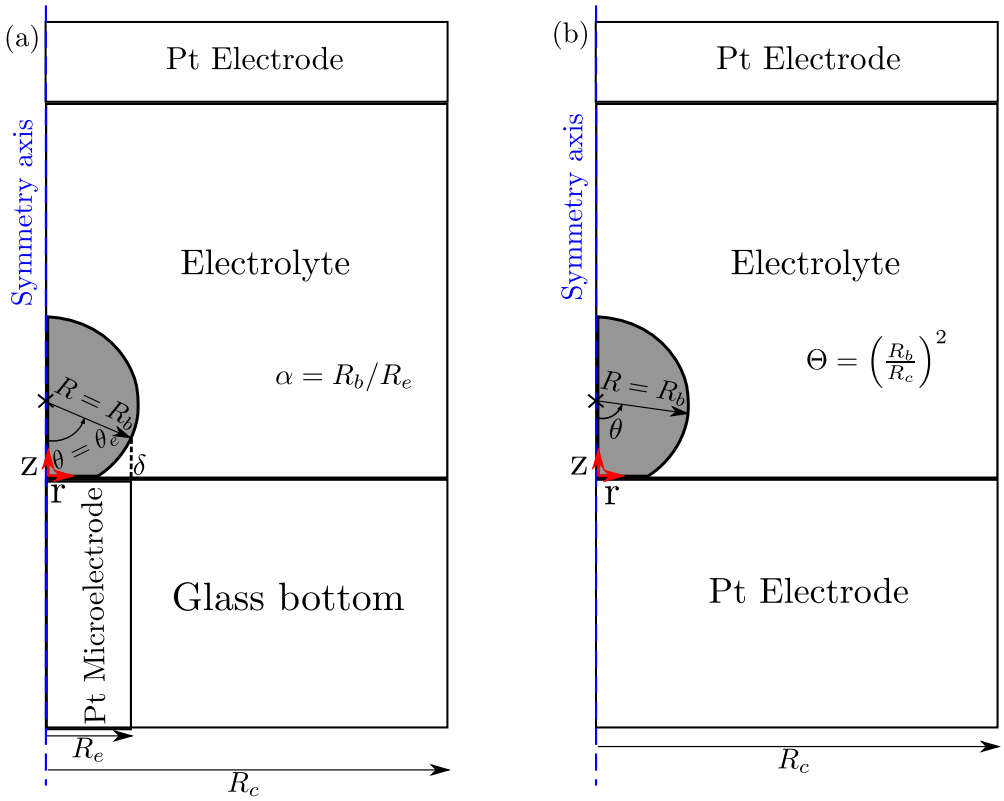

Figure 1: Computational domain (not to scale). a) microelectrode, b) macroelectrode.

and non-uniform heat flux through these domains.

We follow Massing et al. [1] and consider a bubble of fixed size to resemble a late stage of the bubble growth cycle. As shown in Figure 1, we utilize the rotational symmetry of the cell and hence perform axisymmetrical simulations. The leftmost edge in Figure 1 is the axis of symmetry. The following equations to be solved describe the spatial and temporal distribution of the electric potential (ϕ), velocity ($\mathbf{u}$) and temperature (T) in the electrolyte:

$$\nabla^2 \phi = 0 \tag{1}$$

$$\nabla \cdot \mathbf{u} = 0 \tag{2}$$

$$\rho \left(\frac{\partial \mathbf{u}}{\partial t} + (\mathbf{u} \cdot \nabla)\mathbf{u} \right) = -\nabla p + \mu \nabla^2 \mathbf{u} \tag{3}$$

$$\rho C_p \left(\frac{\partial T}{\partial t} + (\mathbf{u} \cdot \nabla)\, T \right) = k \nabla^2 T + \frac{|\mathbf{j}|^2}{\sigma} \tag{4}$$

Here, the primary current density $\mathbf{j} = -\sigma \nabla \phi$ is obtained by solving Eq. (1), where σ denotes the electrical conductivity of the electrolyte, which is assumed to be constant. The electrolyte velocity is obtained by solving the incompressible Navier-Stokes equation (3) complemented by the incompressibility constraint (2),

where p, ρ and μ denote the pressure field and the material properties of density and viscosity. Thermal and solutal buoyancy effects may safely be neglected, as discussed in [1]. The electrolyte temperature is obtained by solving Equation (4), where C_p and k denote the material properties of the specific heat capacity and thermal conductivity. The latter term denotes Joule heating due to electric current passing through the electrolyte. It should be noted here that this term may be neglected in the electrodes, where the electrical conductivity σ is several orders of magnitude larger than in the electrolyte. Therefore, in all other domains (both electrodes, glass bottom and gas bubble), only heat diffusion is solved:

$$\rho C_p \frac{\partial T}{\partial t} = k\nabla^2 T \tag{5}$$

Here, convective heat transport in the gas bubble may safely be neglected, as discussed in [1].

The boundary conditions applied to these equations are as follows: for Equation (1), the electrode surfaces exposed to electrolyte are kept at a fixed potential, i.e. $\phi = 0$ for the working electrode and $\phi = \phi_0$ for the counter electrode. The outer boundary at R_c is electrically insulating, i.e. $\frac{\partial \phi}{\partial \mathbf{n}} = 0$, where $\mathbf{n}$ is the normal unit vector. For Equation (3), a shear stress balance is applied at the electrolyte–bubble interface, i.e. $\tau_H = \tau_M$, where the hydrodynamic shear stress is given by $\tau_H = \mu \left(\nabla \mathbf{u} + (\nabla \mathbf{u})^T\right).\mathbf{n}$, and the thermal Marangoni stress is given by

$$\tau_M = \frac{\partial \gamma}{\partial T}.\nabla_s T \tag{6}$$

Here, γ denotes the interfacial tension, which is assumed to depend on the temperature only, and $\nabla_s \equiv \nabla - (\nabla.\mathbf{n})\,\mathbf{n}$ denotes the gradient along the surface of the interface. As the temperature field is solved in all domains by Eqns. (4) and (5), boundary conditions are required only at the outermost surfaces. The top and the bottom of the computational domain are kept at an ambient temperature $T_{amb} = 20°$ C, while at the outer surface at R_c far from the bubble an adiabatic condition $\frac{\partial T}{\partial \mathbf{n}} = 0$ is applied. Finally, at the symmetry axis at $r = 0$, a zero radial gradient condition is applied on all variables, i.e. $\frac{\partial}{\partial r}(\phi, \mathbf{u}, T) = 0$. The temperature coefficient of the surface tension at the gas-liquid interface is taken to be $\partial\gamma/\partial T = -1.6 \cdot 10^{-4}$ N/m· K [1]. The value of the surface tension γ does not appear directly in our model as the bubble is assumed to be of fixed shape and size. All other material properties are assumed to be constant over the electric potential and temperature range solved for and are shown in Tables 1 and 2.

All equations are solved using the FEM-based simulation software COMSOL 5.4. The initial conditions applied are zero potential, electrolyte at rest and ambient temperature. As discussed extensively in [1], a time integration period of one second was chosen at which nearly stationary and realistic values of the temperature and velocity distribution and the resulting Marangoni force may be expected. To study the effect of the size of the working microelectrode, R_e is varied while R_b is kept constant. We introduce a

Electrolyte	$\mu = 10^{-3}$ Pa·s $\sigma = 40$ S/m $\rho = 10^3$ kg/m^3 $C_p = 4.182$ kJ/kg·K $k = 0.58$ W/m·K

Table 1: Material properties of the electrolyte for Equations 3 and 4

Material	ρ(kg/m^3)	C_p(kJ/kg·K)	k(W/m·K)
Platinum	21450	0.13	72
Glass	2201	1.052	1.38
Hydrogen	0.09	14.32	0.186

Table 2: Material properties for Equation 5

non-dimensional length parameter as the ratio of the bubble radius and the microelectrode radius,

$$\alpha = \frac{R_b}{R_e} \tag{7}$$

As we are here primarily interested in studying how the increasing size of the microelectrode affects the behavior in the vicinity of the gas bubble, unless otherwise mentioned, the radius of the microelectrode is varied from 50 μm to 400 μm such that $R_e < R_b$, i.e. $\alpha > 1$.

Macroelectrode. To study the thermocapillary effect on a large, flat electrode where multiple gas bubbles are growing simultaneously, we take a simplified approach as follows: we first zoom into a small part of the electrode in order to focus only on a single bubble. A cylindrical domain around this bubble is considered, where the radial extension R_c of the domain is half the distance to the next neighboring bubble. We assume that the cell with large electrodes is essentially composed of this periodically repeating domain. Though there are time shifts between the evolution cycles of neighboring bubbles, our simplified approach therefore assumes that all bubbles develop synchronously and also ignores possible coalescence phenomena of neighboring bubbles during growth. A further approximation consists in neglecting azimuthal variations of potential, temperature and velocity which might arise from the finite number of neighboring bubbles sitting at unknown azimuthal positions. This approach treats neighboring effects in an approximate manner averaged over the azimuthal direction and allows the problem to be simulated axisymmetrically. We can therefore make use of the axisymmetric computational domain shown in Figure 1b, which is similar to the one used previously for the microelectrode shown in Figure 1a, and which only needs minor modifications: at the bottom of the cell, the outer glass part is removed, and the electrode is now enlarged over the full radial extent of the cell R_c. At the outer radial boundary, the conditions of electrical insulation for the

potential and an adiabatic condition for the temperature remain unchanged, but in the case of the velocity, vertical slip is applied. The governing equations to be solved for remain as before. In order to quantify the ratio between the bubble size and the size of the cell, we introduce

$$\Theta = \left(\frac{R_b}{R_c}\right)^2 \tag{8}$$

In the framework of our approach, this ratio describes the bubble coverage of the electrode which is defined as the ratio of the bubble area projected on the electrode and the electrode surface area. We can later simply change the bubble coverage of the electrode (which is known to depend on e.g. the mean current density), for example by varying the radial extension of the cell while retaining a fixed bubble size.

3. Results and Discussion

3.1. Microelectrode

3.1.1. General overview

It is evident from Equation 4 that the electrolyte is heated because of the electric current passing through the cell. This causes a temperature gradient along the bubble interface which gives rise to Marangoni flow. Therefore, the current distribution near the interface strongly influences the temperature and flow distribution in the electrolyte. Figure 2(a) shows numerically obtained current lines near the interface for $\alpha = 11.2$. As the gas bubble is electrically insulating, current must pass around it to converge at the microelectrode. Therefore, as the entire cell current must squeeze through a narrow wedge-like region at the bubble foot, the local current density there is very high. In addition, the presence of the bubble makes the outer region of the electrode more accessible to the electric current. This causes an inhomogeneous distribution of the current density over the electrode surface wetted by the electrolyte, as shown in Figure 2(b) for different microelectrode sizes. Here, the cell voltage was kept constant at $\phi_0 = 4.5$ V, and the radial position on the microelectrode is presented normalized by the electrode radius, i.e. $r^* = r/R_e$. As the current density is shown on a logarithmic scale, it clearly can be seen that it varies quite strongly over the radial electrode position and is largest at the electrode periphery. The smaller the microelectrode becomes, the stronger the radial variation of the current density and also its maximum value at the electrode periphery.

As the rate of heat generation scales with the current density squared ($|\mathbf{j}|^2$), the electrolyte experiences strong heating near the periphery of the electrode. Figure 3 shows a zoomed view of the distribution of the temperature rise ($\Delta T = T - T_{amb}$) in the vicinity of the outer electrode edge for $R_e = 200\,\mu$m ($\alpha = 2.8$). It can be seen that the temperature maximum occurs just above the microelectrode periphery at $r^* = 1$. As the surface tension of the bubble interface decreases with increasing temperature, the electrolyte is pulled towards colder parts of the interface, thus establishing an interfacial flow away from the point of maximum temperature. As this bidirectional interfacial flow must be replenished from the bulk, a double-vortex

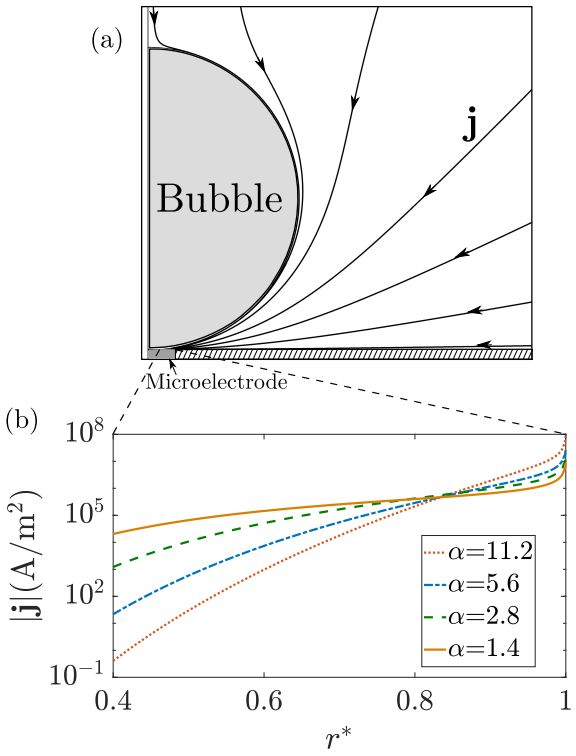

Figure 2: (a) Current lines near the bubble interface as obtained from a simulation for $\phi_0 = 4.5$ V and $\alpha = 11.2$. (b) Distribution of the magnitude of the current density ($|\mathbf{j}|$) on microelectrodes of different size versus the radial position on the wetted part of the electrode normalized with the electrode radius ($r^* = r/R_e$). $\phi_0 = 4.5$ V. $|\mathbf{j}|$ is shown in log scale.

structure is created, as shown for the first time in Figure 3. As will be elaborated in the following, this double-vortex structure is a characteristic feature of the thermocapillary flow driven at the interface of an electrogenerated bubble. In the case of microelectrodes, for geometric reasons, the temperature hotspot appears above the electrode periphery, thus confining the left vortex, and the thermocapillary effect is dominated by the large right vortex. The small size of the left vortex explains, why it was not observed during earlier work at microelectrodes [1].

3.1.2. Interfacial temperature and velocity profile

We now discuss the interfacial temperature and velocity profiles at electrodes of different sizes R_e while the cell voltage is kept constant at $\phi_0 = 4.5$ V. It is to be noted here that, at constant voltage, the electrical resistance of the cell decreases and hence the cell current increases when the microelectrode is enlarged. The obtained profiles of the temperature increment ΔT and tangential velocity ($u_t = \mathbf{u} \cdot \mathbf{t}$) along the bubble interface are shown in Figure 4, with the definition of the angular position θ based on Figure 1. Starting from the point of contact between the bubble and electrode ($\theta_c = 4.2°$), an initial temperature increment is seen in all cases. The smaller the microelectrode is, i.e. the larger α is, the steeper the increase in

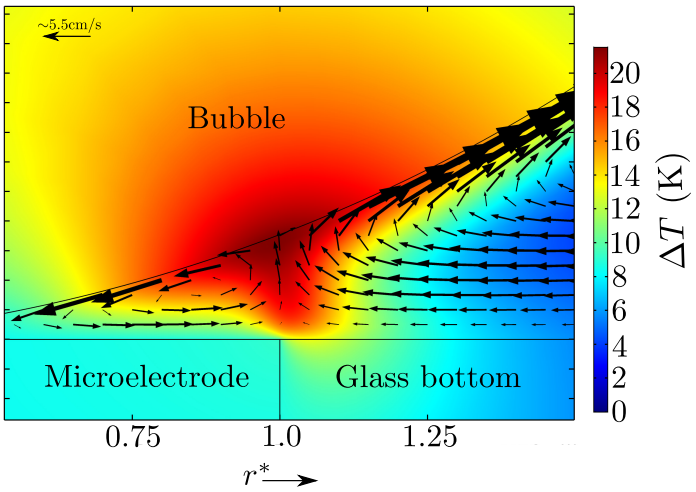

Figure 3: Color contours of the temperature distribution ($\Delta T = T - T_{amb}$) and related electrolyte flow pattern (black: velocity vectors) near the temperature hotspot for a microelectrode of $R_e = 200\,\mu$m ($\alpha = 2.8$) at potential $\phi_0 = 4.5$ V. The radial coordinate is $r^* = r/R_e$.

temperature becomes. At the same time, the angle θ_m at which the maximum temperature increase ΔT_m is observed reduces. This behavior can qualitatively be understood from the discussion on the temperature hotspot in the section above: this was found to be located approximately above $r^* = 1$. Therefore, when the microelectrode grows in size, θ_m also increases. A more detailed discussion on θ_m is given in Section 3.1.3. Moving further along the interface away from θ_m, ΔT gradually decreases towards the bubble north pole at $\theta = 180°$. This general trend in the interfacial temperature profile is seen for all cathode sizes investigated.

It is also to be noted here that the variation of ΔT_m with α is not monotonic. This is because increasing R_e while keeping ϕ_0 constant increases the cell current. Thus the total heat generation in the cell increases, which tends to increase the peak interfacial temperature. As the electrode gets bigger, more heat is carried away by the Pt microelectrode. Greater heat advection from the hotspot by the electrolyte (cf. Figure 4(b)) also contributes similarly. These effects tend to reduce ΔT_m. As a result of the combined action of greater heat generation and higher heat transfer, ΔT_m varies non-monotonically with R_e and thus α. Hence we can see from Figure 4(a) that ΔT_m first increases and then decreases to an almost constant value with a larger electrode i.e. smaller α.

The non-uniform interfacial temperature profile causes thermocapillary stress as shown in Equation 6. Because of the stress balance at the interface, $\tau_M = \tau_H \sim \frac{\partial u_t}{\partial \theta}$, where u_t denotes the tangential velocity at the interface, a Marangoni flow is driven, as already mentioned in Section 3.1.1. The interfacial flow profiles for different microelectrode sizes are shown in Figure 4(b) and can be understood by applying the following sequence of reasoning: According to Equation 6, when the negative temperature coefficient of the surface tension of the electrolyte mentioned in Section 2 is taken into account, positive or negative slopes

of the temperature profile cause negative or positive thermocapillary stress, respectively. Hence, because of the stress balance, the tangential velocity of the Marangoni flow becomes negative or positive, respectively. Consequently, as the flow is purely driven by thermocapillarity, the temperature hotspot separates a region of negative tangential velocity at small angles from a region of positive tangential velocity at larger angles. At the temperature hotspot θ_m itself, the tangential velocity must vanish, i.e. $u_t = 0$. In Figure 4 and later also in Figure 5, an exemple of this is emphasized for the case $\alpha = 5.6$ by a vertical black line . The two regions of velocity of opposite sign are the interfacial parts of the two counter-rotating vortices already seen in Figure 3. As the microelectrode increases in size, the region of negative velocity also increases, yielding a larger vortex above the microelectrode. At the same time, the extremum positions of maximum negative and positive interfacial velocity are both shifted towards larger angles. During this process, the maximum negative velocity decreases monotonically in amplitude, with the initially growing maximum velocity later seeming to level out near a value of about 15 cm/s for $\alpha \sim 1$. However, the total kinetic energy at the interface reaches a maximum at the largest microelectrode size, a straightforward example of the above argument of maximum heat generation at smallest α.

The interfacial temperature distribution at the bubble is determined by the interplay between the generation of heat and the diffusion and advection of heat. For the case of a constant cell voltage (ϕ_0) considered above, all these quantities vary with varying electrode size (α). In order to partly decouple these effects, in the following we study the case of a constant electric cell power which mainly (apart from kinetic losses) determines the generation of heat by Joule dissipation. The total electric power of the cell is given by $P = \phi_0 I_c$, where I_c is the cell current, which in the simulations was determined by integrating the normal current density over the counter-electrode surface ($I_c = \int j_n dA$). In the following, the electrical power is kept constant at $P = 13.4$ mW and α is varied. This power value chosen is the same as the constant cell voltage case at $\alpha = 11.2$, i.e. for the smallest electrode. Hence, the constant cell potential and constant cell power cases are identical for $\alpha = 11.2$. This way, a major remaining factor determining $\Delta T(\theta)$ along the bubble interface is the heat carried by the Pt microlelectrode, which increases with decreasing α. The simulation results are shown in Figure 5. The interfacial temperature profile still maintains the characteristics seen in Figure 4(a). However, because the heat generation is kept constant and the heat carried away from the electrolyte increases along with the electrode size, ΔT_m decreases monotonically with decreasing α, as seen in Figure 5(a). Accordingly, the extrema of maximum negative and positive interfacial velocity eventually decrease monotonically with decreasing α, as seen in Figure 5(b). The same holds for the total kinetic energy at the interface.

3.1.3. Position of the temperature hotspot

As mentioned in Section 3.1.2, the reversal of the direction of interfacial flow coincides with the location of the temperature maximum ΔT_m at the angular position θ_m. It can be further seen in Figure 3 that

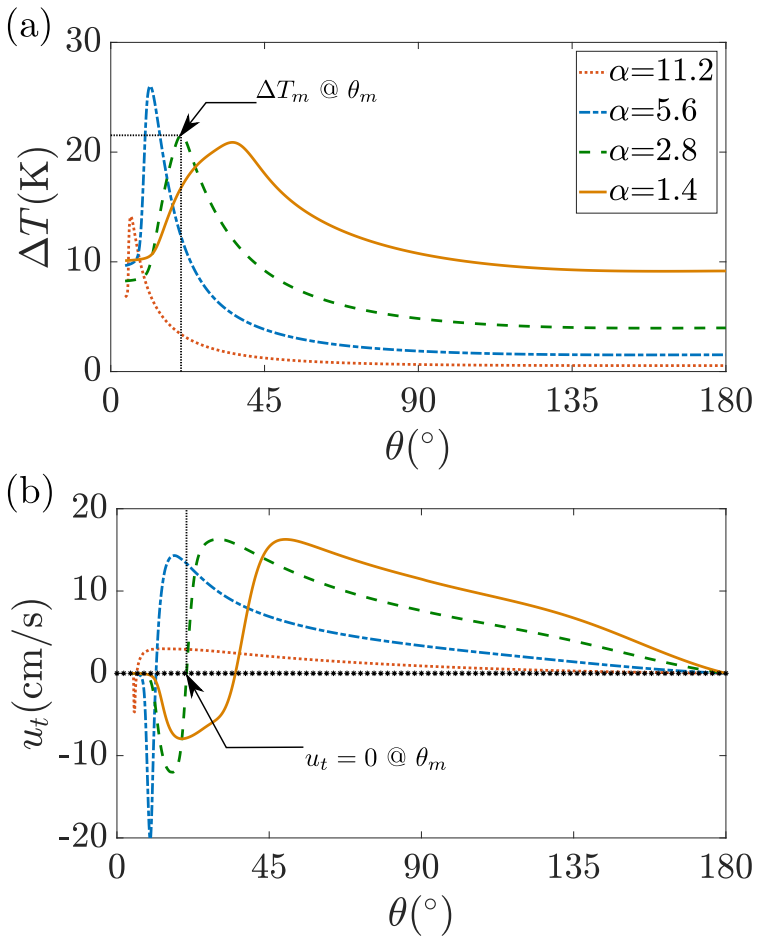

Figure 4: Constant cell voltage case: interfacial temperature (a) and tangential velocity (b) profile as a function of angular position for different electrode sizes expressed by $\alpha = R_b/R_e$

for $\alpha = 2.8$ the position of ΔT_m coincides with the upward projection of the microelectrode's outer edge ($r^* = 1$) onto the bubble interface, as shown in Figure 1. Therefore, we intend to study ΔT_m closer to see whether this geometrical interpretation also holds true for other microelectrode sizes. The angular position of the projection of the microelectrode's outer edge ($r^* = 1$) on the bubble interface is given as

$$\theta_e = \sin^{-1}(R_e/R_b) = \sin^{-1}(1/\alpha)\,. \tag{9}$$

Figure 6 displays the angular position of the interfacial temperature maximum θ_m versus the inverse relative electrode size $\alpha = R_b/R_e$ as obtained from simulations for the cases of constant cell voltage (Figure 4a) and of constant cell power (Figure 5a) in comparison with the values θ_e obtained from the geometrical approach by Equation 9. At small relative electrode size, i.e. at large α, the simulation results for both cases perfectly match with the geometrical relation from Equation 9, which provides a very accurate estimate of the location of the temperature maximum at the interface. As the microelectrode increases in size, only small differences

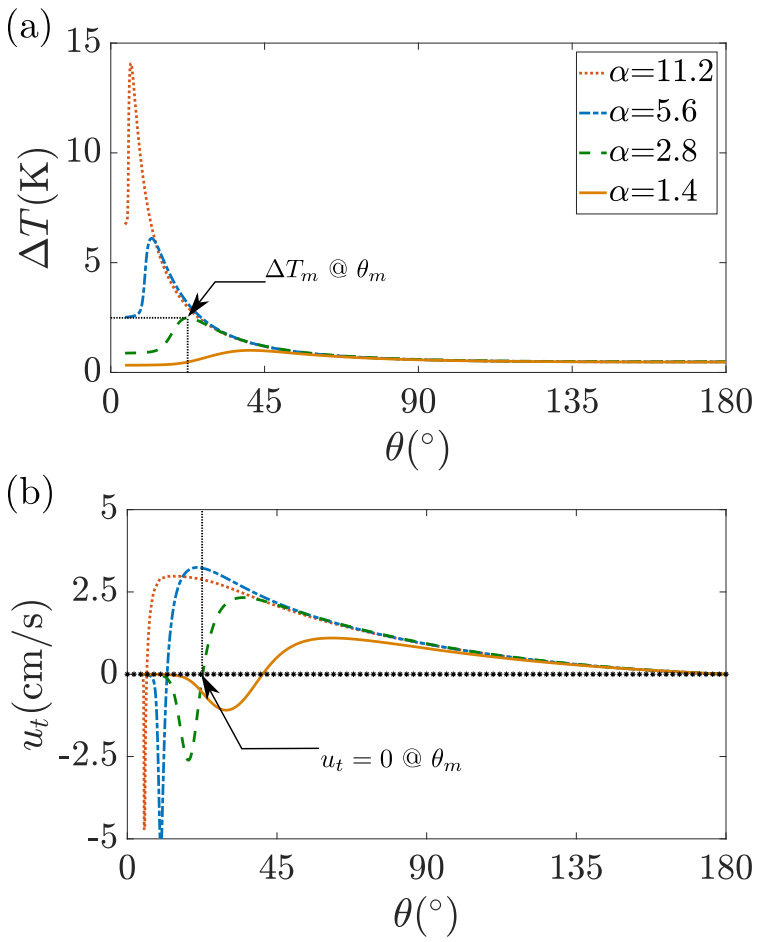

Figure 5: Constant cell electric power ($P = 13.4$ mW) case: interfacial temperature (a) and velocity (b) profile as a function of the angular position for different electrode sizes expressed by $\alpha = R_b/R_e$

are seen between the two simulation cases, besides an overall good match being maintained with Equation 9. Eventually, at $\alpha = 1.2$, both cases seem to deviate from the analytical curve and deliver smaller angular positions of the temperature hotspot than Equation 9. This is caused by the fact that as the microelectrode increases in size, as seen from Figure 2, the non-uniformity of the current density, i.e. the ratio of the peak value at the electrode edge in comparison to the mean value, decreases. Therefore, as α approaches unity, inner parts of the electrode surface also contribute to the generation of the temperature hotspot, which leads to the observed slight shift in the position of the temperature maximum towards smaller angular positions. In summary, the geometrically estimated angular position θ_e of the temperature maximum θ_m based on the inhomogeneous distribution of the current density at the microelectrode provides a useful estimation of the position of the temperature maximum θ_m and the resulting interfacial flow characteristics at the bubble interface at the microelectrode without the need to perform detailed simulations or experimentation. We would also like to point out here that Equation 9 is only valid for $R_e \leq R_b$, which coincides with the range

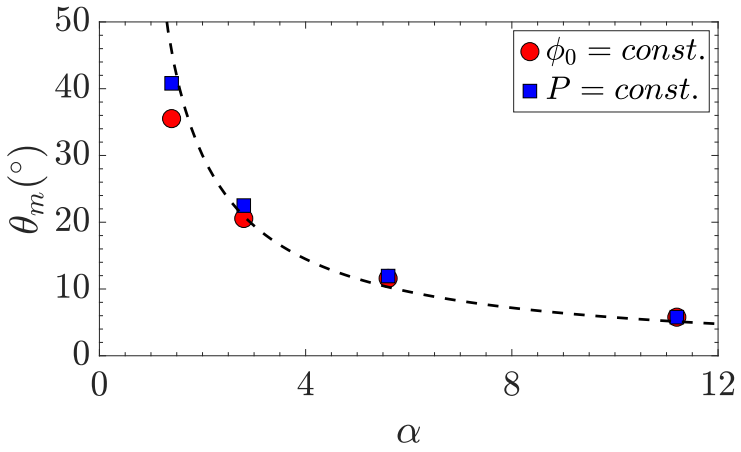

Figure 6: Angular position of the interfacial temperature maximum (θ_m) versus $\alpha = R_b/R_e$ at fixed $R_b = 560\,\mu$m for the cases of constant cell voltage (red circles) and of constant cell power (blue squares). The dashed curve denotes the geometrical relation from Equation 9.

of studies for the microelectrode case presented here.

3.1.4. Marangoni force

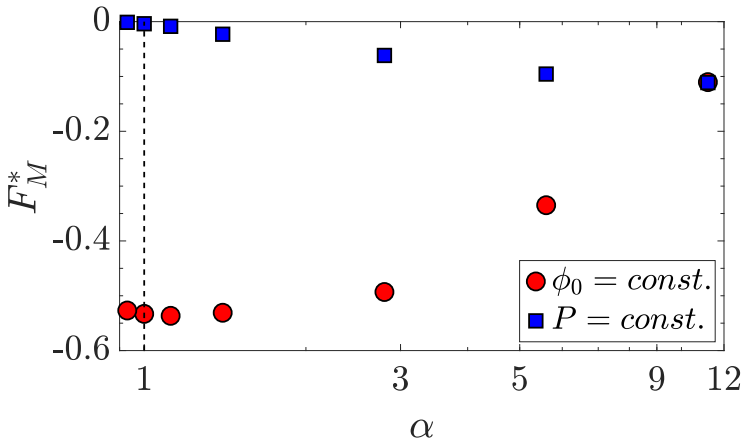

Figure 7: Marangoni force acting on the bubble, shown as normalized by the buoyancy force ($F_M^* = F_M/F_B$), at different values of $\alpha = R_b/R_e$. The $x-$axis is shown in logarithmic scale to emphasize the behavior at low α. In the case of constant cell voltage, $\phi_0 = 4.5$ V. In the case of constant cell power, $P = 13.4$ mW.

We now focus on investigating the resulting thermocapillary force on the bubble at different microelectrode sizes. As already mentioned in the introduction, the moment of bubble detachement is determined by the equilibrium of forces acting on the bubble. Therefore, a comprehensive treatment of all the forces acting on a bubble is of importance. A number of different forces may act on the bubble depending on

the predominant physical conditions i.e. growth rate, imposed flow condition, orientation relative to gravity, etc. [34] The relevant static forces acting on an electrogenerated bubble are in general the buoyancy force, surface tension force, contact pressure force and hydrodynamic force originating from the flow of the electrolyte [42, 43]. Recently it was shown that beside the thermocapillary force [1], an electrostatic force may also play an important role [44].

The thermocapillary force on the bubble is a hydrodynamical force by nature and results from the interfacial flow around the bubble driven by temperature gradients. In the following, we will denote the force as the Marangoni force, which can be calculated by integrating the Marangoni shear stress over the bubble interface (Σ),

$$F_M = -\int_\Sigma \tau_M dA. \tag{10}$$

Here, dA denotes the related surface differential. Because of the axial symmetry around the bubble, the above integration results in a force which is acting parallel to the $z-$axis, i.e. vertically upwards or downwards, thus influencing the moment of detachment. In the following, we consider the Marangoni force F_M in relation to the buoyancy force $F_B = gV\Delta\rho$ where g, V and $\Delta\rho$ denote the gravitational acceleration, the bubble volume and the density difference between the electrolyte and gas, respectively. Thus, we introduce

$$F_M^* = \frac{F_M}{F_B} \tag{11}$$

where positive values of F_M^* imply a Marangoni force acting in the direction of buoyancy.

Figure 7 shows the dependence of F_M^* on the inverse relative electrode size (α) at a constant cell voltage and constant cell electric power. Note that the differential local Marangoni force experienced by any part of the interface is opposite to the direction of local interfacial velocity. According to the velocity profiles shown in Figure 4(b) and 5(b), the lower part of the bubble ($\theta < \theta_m$) experiences a net Marangoni force in the upward direction and the upper part of the bubble experiences a net Marangoni force in the downward direction. As for the microelectrode, the extent of the flow vortex to the left of temperature hotspot is smaller than that to the right of the temperature hotspot. The integration of Equation 10 gives a net F_M in the downward direction, hence F_M^* is negative at large α. For the potentiostatic case, as with decreasing α, the mean current density and thus the heat generation in the electrolyte grows, F_M^* also increases in magnitude. When decreasing α further, the growing contribution from the left vortex becomes more and more important, and F_M^* starts to decrease in magnitude near $\alpha \sim 1$. We further see that at $\alpha \sim 1$, due to very strong heating, the Marangoni force has reached a magnitude of roughly 55% of buoyancy, which corresponds to a very large mean current density value of 34.8 A/cm^2.

As the electrode size is increased while keeping the total heat generation constant, the temperature nonuniformity along the interface reduces and the contribution from the two vortices becomes comparable. Thus, F_M^* decreases with decreasing α, becoming approximately zero at $\alpha \sim 1$.

3.2. Macroelectrode

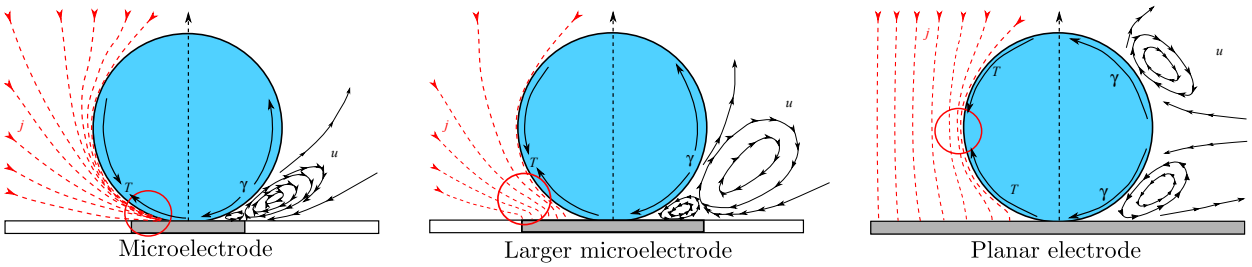

Figure 8: Sketch depicting the qualitative differences in current distribution, position of temperature hotspot (red circle) and resulting thermocapillary flow pattern when the size of the electrode is increased from micro (left) to macro (right). The flow inside the gas bubble and the movement of the interface are not shown.

So far we have presented a detailed characterization of the thermocapillary effect on gas bubbles growing at microelectrodes of different sizes. As larger electrodes are prevalent in industrial processes, an in-depth understanding of similar phenomena at macroelectrodes is of technological importance. An attempt is made here to gain an understanding of this kind for the first time. With respect to the modeling, we follow the simple approach described in detail in Section 2, based on considering single bubble phenomena, and originating from the previous study of microelectrodes after accounting for differences in length scales and boundary conditions.

Figure 8 schematically displays important qualitative differences of the thermocapillary effect when the size of the electrode is increased from micro (left) to macro (right) with respect to the bubble size. For the sake of simplicity, at the macroelectrode only a small part of the electrode is shown, above which a single bubble evolves. Looking at the distribution of the current density, shown by red dotted lines, important differences become obvious. At the microelectrode, as discussed before, the current has to squeeze through a narrow region at the bubble foot, and large current densities occur above the electrode, with a maximum near its outer edge. In the center of the figure, the intermediate case of a large microelectrode is shown, where, as discussed before, the temperature hotspot has already moved upward slightly towards a larger value of θ. At the macroelectrode, however, the situation is changed, as the main geometrical obstacle for a uniform current flow is now the bubble itself and not the electrode. Here, the current has to pass the narrower equatorial space between neighboring bubbles. Hence, the maximum of the current density appears at the bubble's equator. As the position of the temperature hotspot correlates directly with the location of the maximum current density, the temperature maximum moves from the bubble foot towards the bubble equator when the size of the electrode is increased from micro to macro.

The thermocapillary flow patterns driven at the bubble interface from hot towards cold regions are sketched in the right half of the subfigures for all three cases. In line with the changing position of the temperature hotspot, the size and the position of the two counter-rotating vortices driven by thermocapillary stress

change accordingly. At the microelectrode, a dominating large vortex brings electrolyte upward along the interface, and the small vortex above the electrode does not contribute much to the thermocapillary effect. This small vortex grows in size when the size of the microelectrode is increased and starts contributing to the Marangoni force on the bubble, as already discussed in the previous section. At the macroelectrode, eventually, two counter-rotating vortices of almost equal size are therefore expected which advect electrolyte away from the temperature hotspot at the equator. The ramifications of these qualitative changes are investigated quantitatively in the following.

3.2.1. Temperature and velocity distribution

We now study in detail the temperature and velocity distribution near a gas bubble of constant size ($R_b = 560\,\mu$m) at different values of the bubble coverage Θ of the macroelectrode. In the following, a potential difference of $\phi_0 = 1\,V$ is applied between the electrodes. We note that, e.g. for a bubble coverage of $\Theta = 0.87$, an average current density of 4.9 kA/m^2 is obtained, which is close to typical values of 1–3 kA/m^2 in related industrial applications [30]. Figure 9(a) shows the temperature distribution in and around

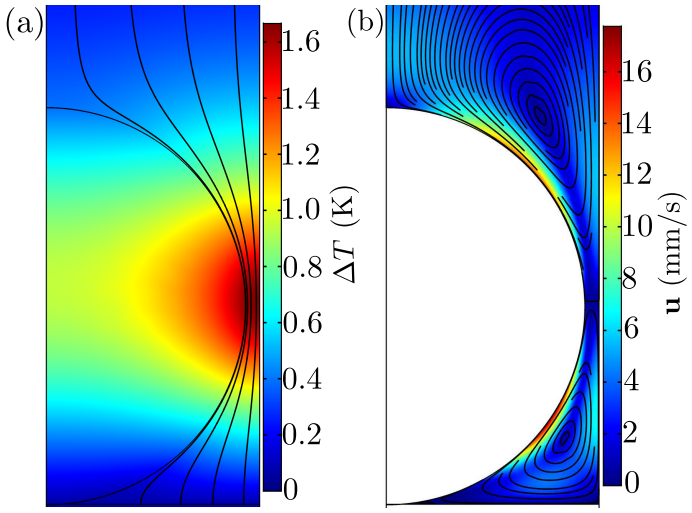

Figure 9: ($\phi_0 = 1$ V and $\Theta = 0.87$) (a) Temperature contours and field lines of the electrical current density. Temperature is maximum at the location of maximum current density near bubble equator. (b) Contours of the electrolyte flow velocity distribution along with velocity streamlines. The electrolyte at the bubble interface flows away from the equator towards both poles.

the gas bubble at a bubble coverage of $\Theta = 0.87$. As can be seen from the current lines in the electrolyte, the electric current must pass around the gas bubble and hence is highly concentrated in the narrow inter-bubble region near the bubble equator, where the largest current density occurs, in agreement with the expectations formulated in the previous section. The temperature maximum also occurs at the same spot, as can be seen from the temperature distribution.

Figure 9(b) shows the velocity distribution and the streamlines in the electrolyte. The thermocapillary flow is driven away from the temperature hotspot, and the electrolyte flows away from the equator towards either pole. This gives rise to two vortices in the northern and southern hemisphere of the bubble and causes two interfacial velocity maxima, visible as the red regions in Figure 9(b). It is also to be noted here that the vortices are not fully symmetric with respect to the equatorial plane. The lower vortex is constrained by the electrode surface, the bubble interface and the outer boundary of the domain, whereas the upper vortex extends upward above the top of the bubble.

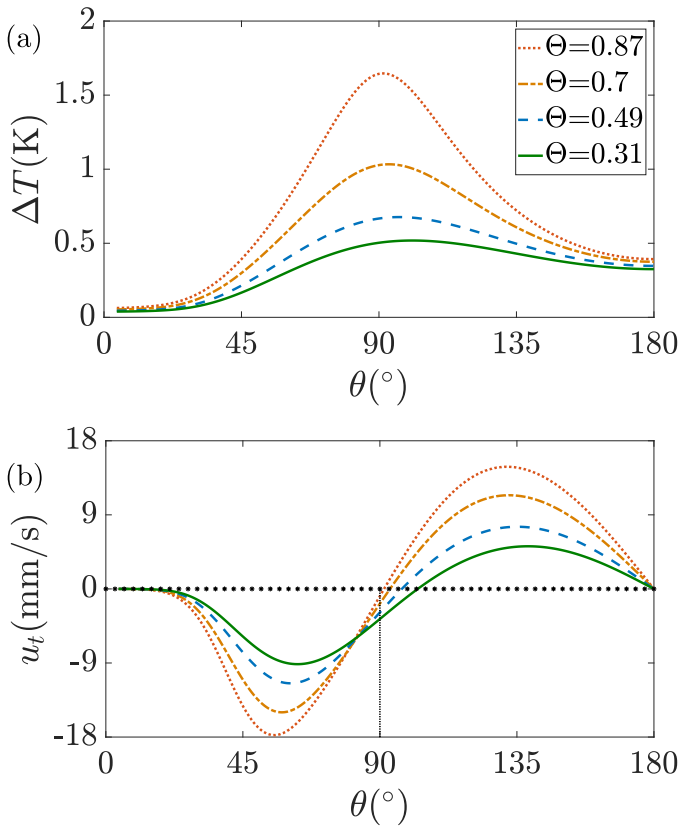

Figure 10: Interfacial (a) temperature and (b) velocity distribution as a function of θ as defined in Figure 1 for different electrode coverage Θ at $\phi_0 = 1$ V. The vertical dashed line marks $\theta = 90°$.

Next we study in detail the influence of the bubble coverage on the interfacial temperature and flow profiles. R_c is varied from 0.6 mm to 1 mm, yielding a range of Θ from 0.87 to 0.31, which, according to earlier work, provides a realistic range of gas coverage values [45]. Figure 10(a) shows the interfacial temperature profile as a function of the angular position θ. The occurrence of a temperature maximum close to the bubble equator ($\theta_m \sim 90°$) is clearly visible in all cases. The temperature maximum also increases with increasing bubble coverage, as the electric current lines are more densely placed in the inter-bubble space, causing larger local Joule heating. Figure 10(b) shows the related interfacial velocity profile.

Similarly to the microelectrode case discussed in Section 3.1.2, the tangential velocity u_t vanishes at the position of the temperature maximum at θ_m. According to the slopes of opposite sign in the temperature profile left and right of θ_m, interfacial flow in the southern or northern hemisphere is directed downward and upward, respectively, as also shown in Figure 10(b). In this figure, the value of zero tangential velocity $u_t = 0$ and the angular position of the equator $\theta = 90°$ are additionally marked by lines to allow the more accurate identification of the location of the flow reversal (θ_m) in relation to the bubble equator. As can be seen, the temperature hotspot is slightly shifted above the equator at smaller bubble coverage values. Furthermore, it is to be noted that the magnitude of the velocity minimum in the southern hemisphere is larger than the magnitude of the velocity maximum in the northern hemisphere in general. The latter can easily be explained. As the metal electrode at the bottom is a good conductor of heat compared to the electrolyte, the related downward heat flux tends to increase the temperature gradient in the southern hemisphere, leading to a larger velocity magnitude. This larger velocity magnitude also causes enhanced advection of heat at the interface, which leads to a shift in the temperature hotspot above the equator. As increasing the bubble coverage narrows the gap between the bubble equator and domain boundary, the temperature hotspot at the equator increases, and the relative influence of cooling and advection reduces. This is also seen in the two extrema of the velocity profiles, which grow closer to each other in terms of magnitude.

3.2.2. Marangoni force on the bubble

It is well known from measurements on large planar electrodes that the bubble evolution characteristics depend on the operating current density [45, 46]. At a higher current density, more nucleation sites are activated at the electrode, and thus the bubble coverage increases. Increasing the average current density also reduces the departure diameter and causes early detachment from the electrode surface [47]. In order to discuss the possible influence of thermocapillary effects on these phenomena, we carried out parametric studies to elaborate the influence of varying bubble coverage and bubble size on the Marangoni force under different operating conditions. The results are shown in Figure 11.

Constant bubble radius. In Figure 11(a) the Marangoni force normalized with the buoyancy force F_M^* (as defined in Section 3.1.4) is shown versus the bubble coverage of the electrode Θ for a gas bubble of fixed size ($R_b = 560\,\mu$m) at a constant cell voltage of $\phi_0 = 1\,V$. It should be noted first that unlike the case of the microelectrode considered earlier, the Marangoni force is directed upwards, thus advancing the bubble departure. The Marangoni force F_M^* is found to amount to about 2% of the buoyancy force in the range of parameters considered and increases almost linearly with the bubble coverage Θ.

As the Marangoni force (F_M) results from the integration of the interfacial temperature gradient along the interface (see Equation 10), the slight asymmetry of the interfacial temperature profile with respect to the equator seen in Figure 10(a) gives rise to a remaining nonzero force F_M. As the temperature gradient

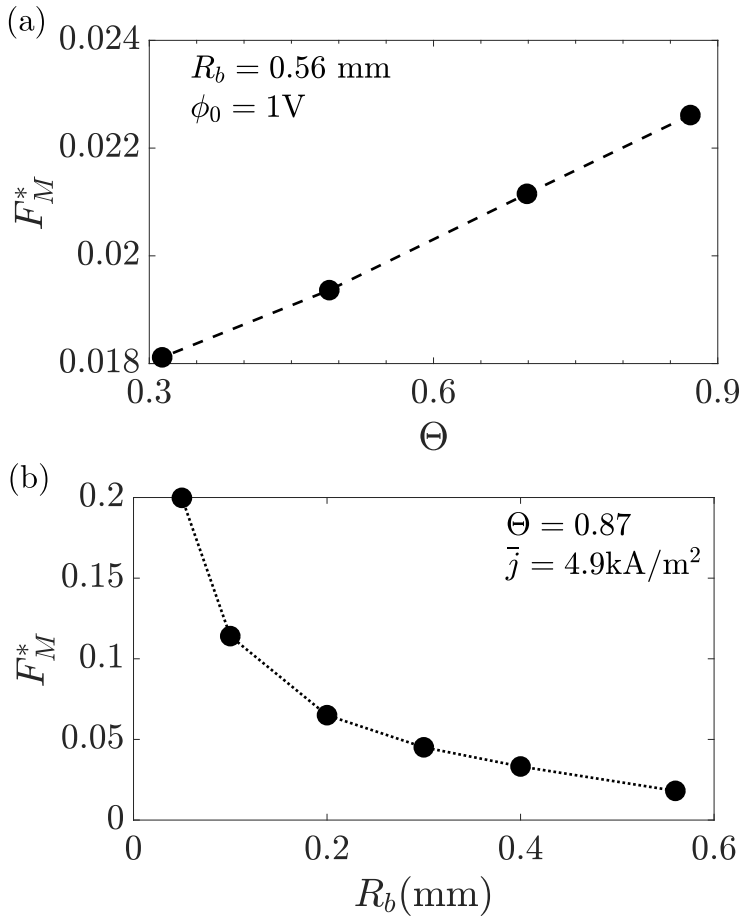

Figure 11: Marangoni force normalized with buoyancy force F_M^* versus (a) bubble coverage Θ at a constant bubble radius $R_b = 560\,\mu$m and cell voltage $\phi_0 = 1$ V and versus (b) bubble radius R_b at a constant bubble coverage $\Theta = 0.87$ and mean cell current density $\bar{j} = 4.9$ kA/m^2.

is negative in the region below the equator and larger in magnitude than the positive gradient above the equator, eventually an upward Marangoni force appears. The almost linear increase in the Marangoni force as the bubble coverage increases is related to the strong temperature increase of the hotspot near the equator in conjunction with the heatflux through the electrode, thus retaining a steep temperature profile below the equator.

Constant bubble coverage. In order to extend our study to include smaller gas bubble departure sizes, Figure 11(b) summarizes the Marangoni force F_M^* obtained for different bubble radii R_b at a constant bubble coverage of $\Theta = 0.87$ and at mean cell current density of $\bar{j} = 4.9$ kA/m^2. We would like to point out here that smaller bubbles have shorter residence times [47]. This was taken into account by adapting the integration time in the simulations accordingly. The simulation details are summarized in Table 3. Starting

out from an integration time of 1 s at $R_b = 560\,\mu$m in accordance with the constant bubble radius case considered earlier, the integration time is then linearly decreased along with the bubble size such that for a bubble of 200 μm radius it matches the bubble lifetime of about 0.4 s reported in [48]. Please also note that for smaller bubbles the contact angle between the bubble and electrode was slightly increased. As can be seen in Figure 11(b), the Marangoni force F_M^* strongly increases when the size of the bubble reduces. This behavior is mainly caused by the corresponding variation in the buoyancy force, which scales with the cube of the bubble size. For a small bubble of $R_b = 50\,\mu$m, the Marangoni force is found to amount to about 20% of the buoyancy force.

R_b (μm)	θ_c	Integration Time (s)
50	14.1°	0.15
100	9.9°	0.23
200	7.0°	0.4
300	5.7°	0.57
400	5.0°	0.73
560	4.2°	1.0

Table 3: Bubble radius, contact angle and integration time in the simulation

4. Conclusions

In this study we characterized in detail the thermocapillary flow around electrogenerated bubbles at electrodes of different sizes, ranging from microelectrodes to large planar electrodes. At microelectrodes, a detailed analysis of the current density and temperature profiles revealed a clear correlation between the position of the temperature hotspot at the bubble interface and the upward projection of the outer edge of the microelectrode. As a result, a double vortex structure of the thermocapillary flow was unveiled which was overlooked previously [1] because the lower vortex is small at the microelectrodes. This double vortex structure is also found at larger electrodes. Increasing the electrode size changes the position of the temperature hotspot, thus increasing the size of the lower vortex and affecting the amplitude and also the direction of the Marangoni force.

At large planar electrodes, multiple bubbles grow simultaneously at random nucleation sites where the electrical current must pass through the inter-bubble space. The simplified approach we take in order to gather initial results assumes that the bubbles grow synchronously at a given uniform nucleation density, meaning that a single bubble can only be considered in the simulations. As a result, the maximum current density and thus the temperature hotspot are located close to the equatorial inter-bubble region, and a nearly symmetric double vortex structure is generated near the bubble interface. However, mainly because

of the cooling effect of the metal electrode, the interfacial flow of the lower vortex is stronger than that of the upper vortex. Consequently, an upward Marangoni force acts on the bubble, assisting its release, which is the opposite of what is found at the microelectrodes. This clearly helps explain why larger bubbles can be grown on macroelectrodes compared to microelectrodes. At a constant cell voltage, the Marangoni force is found to grow as the bubble coverage of the electrode increases due to higher temperatures occurring in the smaller inter-bubble gaps. For a fixed current density and related large bubble coverage, the force on the bubble is found to get larger when the bubble size is reduced, reaching about 20% of the buoyancy force at $\Theta = 0.87$, $\bar{j} = 4.9$ kA/m^2.

We note here that the quantitative results obtained for the macroelectrode are based on the assumption of uniform bubble distribution, i.e. simultaneous in-phase bubble evolution, and that azimuthal dependencies of quantities originating from neighboring bubbles growing at certain angular positions have so far been neglected. The Marangoni force values obtained for reasonable integration times in our model may further depend on the specific value of the contact angle and neglect more complex aspects such as microbubbles partly covering the cathode. It should also be noted that our results for all electrode sizes naturally depend in quantity on the details of the thermal boundary conditions of the cell. This especially holds true for the metal electrode where the bubble grows, which takes heat out of the electrolyte and thereby shapes the thermocapillary effect. Nevertheless, as this is a common feature, we believe the qualitative findings of the thermocapillary effect are valid in general.

In summary, the thermocapillary effect is found to be important for the dynamics of bubbles generated at electrodes under various conditions. A proper inclusion of this effect in future studies may lead to an improved understanding of the instant of the bubble departure and the departure diameter. Finally, appropriate temperature management of the electrodes may be a useful means of improving the efficiency of electrolyzers.

Acknowledgement

We gratefully acknowledge fruitful discussions with Xuegeng Yang. This project is supported by German Aerospace Center (DLR) with funds provided by the Federal Ministry for Economics Affairs and Energy (BMWi) due to an enactment of the German Bundestag under grant no. DLR 50WM1758 (project MADA-GAS).

References

References

[1] J. Massing, G. Mutschke, D. Baczyzmalski, S. S. Hossain, X. Yang, K. Eckert, C. Cierpka, Thermocapillary convection during hydrogen evolution at microelectrodes, Electrochimica Acta 297 (2019) 929–940. doi:10.1016/j.electacta.2018.11.187.

[2] V. Levich, V. Krylov, Surface-tension-driven phenomena, Annual Review of Fluid Mechanics 1 (1) (1969) 293–316. doi:10.1146/annurev.fl.01.010169.001453.

[3] A. W. Adamson, Gast, Physical Chemistry of Surfaces, Wiley-Interscience, 1967.

[4] L. G. Leal, Advanced Transport Phenomena: Fluid Mechanics and Convective Transport Processes, Vol. 7, Cambridge University Press, 2007.

[5] J. Pearson, On convection cells induced by surface tension, Journal of fluid mechanics 4 (5) (1958) 489–500.

[6] D. Nield, Surface tension and buoyancy effects in cellular convection, Journal of Fluid Mechanics 19 (3) (1964) 341–352.

[7] K. Eckert, M. Bestehorn, A. Thess, Square cells in surface-tension-driven bénard convection: experiment and theory, Journal of Fluid Mechanics 356 (1998) 155–197.

[8] K. Schwarzenberger, T. Köllner, H. Linde, T. Boeck, S. Odenbach, K. Eckert, Pattern formation and mass transfer under stationary solutal marangoni instability, Advances in colloid and interface science 206 (2014) 344–371.

[9] H. Hu, R. G. Larson, Analysis of the microfluid flow in an evaporating sessile droplet, Langmuir 21 (9) (2005) 3963–3971.

[10] H. Hu, R. G. Larson, Marangoni effect reverses coffee-ring depositions, The Journal of Physical Chemistry B 110 (14) (2006) 7090–7094. doi:10.1021/jp0609232.

[11] B. J. Fischer, Particle convection in an evaporating colloidal droplet, Langmuir 18 (1) (2002) 60–67.

[12] Á. G. Marín, H. Gelderblom, A. Susarrey-Arce, A. Van Houselt, L. Lefferts, J. G. Gardeniers, D. Lohse, J. H. Snoeijer, Building microscopic soccer balls with evaporating colloidal fakir drops, Proceedings of the National Academy of Sciences 109 (41) (2012) 16455–16458.

[13] N. Young, J. Goldstein, M. J. Block, The motion of bubbles in a vertical temperature gradient, Journal of Fluid Mechanics 6 (3) (1959) 350–356. doi:10.1017/S0022112059000684.

[14] R. Balasubramaniam, R. S. Subramanian, The migration of a drop in a uniform temperature gradient at large marangoni numbers, Physics of Fluids 12 (4) (2000) 733–743.

[15] R. Balasubramaniam, R. Subramaniam, Thermocapillary bubble migration—thermal boundary layers for large marangoni numbers, International journal of multiphase flow 22 (3) (1996) 593–612.

[16] R. Balasubramaniam, C. E. Lacy, G. Woniak, R. S. Subramanian, Thermocapillary migration of bubbles and drops at moderate values of the marangoni number in reduced gravity, Physics of Fluids 8 (4) (1996) 872–880.

[17] J. L. McGrew, F. L. Bamford, T. R. Rehm, Marangoni flow: an additional mechanism in boiling heat transfer, Science 153 (3740) (1966) 1106–1107.

[18] J. Straub, The role of surface tension for two-phase heat and mass transfer in the absence of gravity, Experimental Thermal and Fluid Science 9 (3) (1994) 253–273.

[19] S. Petrovic, T. Robinson, R. L. Judd, Marangoni heat transfer in subcooled nucleate pool boiling, International Journal of Heat and Mass Transfer 47 (23) (2004) 5115–5128.

[20] V. K. Dhir, G. R. Warrier, E. Aktinol, D. Chao, J. Eggers, W. Sheredy, W. Booth, Nucleate pool boiling experiments (npbx) on the international space station, Microgravity Science and Technology 24 (5) (2012) 307–325.

[21] J. Straub, J. Betz, R. Marek, Enhancement of heat transfer by thermocapillary convection around bubbles-a numerical study, Numerical Heat Transfer 25 (5) (1994) 501–518.

[22] R. Marek, J. Straub, The origin of thermocapillary convection in subcooled nucleate pool boiling, International Journal of Heat and Mass Transfer 44 (3) (2001) 619–632.

[23] S. Lubetkin, The fundamentals of bubble evolution, Chemical Society Reviews 24 (4) (1995) 243–250.

[24] S. Lubetkin, The motion of electrolytic gas bubbles near electrodes, Electrochimica Acta 48 (4) (2002) 357–375. doi:10.1016/S0013-4686(02)00682-5.

[25] X. Yang, D. Baczyzmalski, C. Cierpka, G. Mutschke, K. Eckert, Marangoni convection at electrogenerated hydrogen bubbles, Physical Chemistry Chemical Physics 20 (2018) 11542–11548. doi:10.1039/C8CP01050A.

[26] F. Li, R. Gonzalez-Avila, D. Nguyen, C.-D. Ohl, Oscillate boiling from microheaters, Phys. Rev. Fluids 2 (2017) 014007.
[27] W. Tsai, P. Hsu, Y. Hwu, C. Chen, L. Chang, J. Je, H. Lin, A. Groso, G. Margaritondo, Electrochemistry: building on bubbles in metal electrodeposition, Nature 417 (6885) (2002) 139.
[28] J. Jorne, J. F. Louvar, Gas-diverting electrodes in the chlor-alkali membrane cell, Journal of The Electrochemical Society 127 (2) (1980) 298–303.
[29] J. C. Puippe, R. Acosta, R. Von Gutfeld, Investigation of laser-enhanced electroplating mechanisms, Journal of the Electrochemical Society 128 (12) (1981) 2539–2545.
[30] K. Zeng, D. Zhang, Recent progress in alkaline water electrolysis for hydrogen production and applications, Progress in energy and combustion science 36 (3) (2010) 307–326.
[31] A. Körner, C. Tam, S. Bennett, J. Gagné, Technology roadmap – hydrogen and fuel cells, Tech. rep., International Energy Agency (IEA): Paris, France (2015).
[32] I. Staffell, D. Scamman, A. V. Abad, P. Balcombe, P. E. Dodds, P. Ekins, N. Shah, K. R. Ward, The role of hydrogen and fuel cells in the global energy system, Energy & Environmental Science 12 (2) (2019) 463–491.
[33] N. Brandon, Z. Kurban, Clean energy and the hydrogen economy, Philosophical Transactions of the Royal Society A: Mathematical, Physical and Engineering Sciences 375 (2098) (2017) 20160400.
[34] G. Thorncroft, J. F. Klausner, Bubble forces and detachment models, Multiphase Science and Technology 13 (3&4) (2001). doi:10.1615/MultScienTechn.v13.i3-4.20.
[35] W. Fritz, Berechnung des maximalvolumes von dampfblasen, Physik. Zeitschr 36 (1935) 379–384.
[36] D. Fernandez, P. Maurer, M. Martine, J. Coey, M. E. Möbius, Bubble formation at a gas-evolving microelectrode, Langmuir 30 (43) (2014) 13065–13074.
[37] J. Chen, L. Guo, X. Hu, Z. Cao, Y. Wang, Dynamics of single bubble departure from tio2 nanorod-array photoelectrode, Electrochimica Acta 274 (2018) 57–66.
[38] D. E. Westerheide, J. Westwater, Isothermal growth of hydrogen bubbles during electrolysis, AIChE Journal 7 (3) (1961) 357–362.
[39] N. P. Brandon, The growth kinetics and interfacial properties of electrogenerated bubbles, Ph.D. thesis, Imperial College London (1985).
[40] H. Matsushima, D. Kiuchi, Y. Fukunaka, K. Kuribayashi, Single bubble growth during water electrolysis under microgravity, Electrochemistry Communications 11 (8) (2009) 1721–1723.
[41] X. Yang, F. Karnbach, M. Uhlemann, S. Odenbach, K. Eckert, Dynamics of single hydrogen bubbles at a platinum microelectrode, Langmuir 31 (29) (2015) 8184–8193. doi:10.1021/acs.langmuir.5b01825.
[42] A. Taqieddin, M. R. Allshouse, A. N. Alshawabkeh, Editors' choice - critical review - mathematical formulations of electrochemically gas-evolving systems, Journal of The Electrochemical Society 165 (13) (2018) E694–E711. doi:10.1149/2.0791813jes.
[43] D. Baczyzmalski, F. Karnbach, G. Mutschke, X. Yang, K. Eckert, M. Uhlemann, C. Cierpka, Growth and detachment of single hydrogen bubbles in a magnetohydrodynamic shear flow, Physical Review Fluids 2 (9) (2017) 093701.
[44] A. Bashkatov, S. S. Hossain, X. Yang, G. Mutschke, K. Eckert, Oscillating hydrogen bubbles at pt microelectrodes, Physical Review Letters 123 (2019) 214503. doi:https://doi.org/10.1103/PhysRevLett.123.214503.
[45] H. Vogt, On the supersaturation of gas in the concentration boundary layer of gas evolving electrodes, Electrochimica Acta 25 (5) (1980) 527–531.
[46] H. Vogt, R. Balzer, The bubble coverage of gas-evolving electrodes in stagnant electrolytes, Electrochimica Acta 50 (10) (2005) 2073–2079.
[47] H. Vogt, The actual current density of gas-evolving electrodes—notes on the bubble coverage, Electrochimica Acta 78 (2012) 183–187.

[48] H. Matsushima, T. Iida, Y. Fukunaka, Gas bubble evolution on transparent electrode during water electrolysis in a magnetic field, Electrochimica Acta 100 (2013) 261–264.